aerospace

MDPI

Article

Adaptive Vibration Control for Helicopter with Active Rotor Using Double-Acting Piezoelectric Actuator

Xiancheng Gu [1], Weidong Yang [1], Linghua Dong [1,*] and Jinlong Zhou [2]

[1] National Key Laboratory of Helicopter Aeromechanics, Nanjing University of Aeronautics and Astronautics, Nanjing 210016, China; gxc2020@nuaa.edu.cn (X.G.); ywdae@nuaa.edu.cn (W.Y.)
[2] College of General Aviation and Flight, Nanjing University of Aeronautics and Astronautics, Changzhou 213300, China; zhoujinlong101@nuaa.edu.cn
* Correspondence: donglinghua@nuaa.edu.cn

Abstract

Active rotors with trailing-edge flaps (TEFs) are a promising method applied to the main-rotor blades of the helicopter for vibration suppression. For active rotors, both the TEF actuator and the corresponding deflection control law determine their overall performance and effectiveness for vibration reduction. In this study, a double-acting piezoelectric actuator is designed to actuate the TEFs, where bidirectional push/pull output is achieved by two groups of piezoelectric stacks operating in opposite directions. Benchtop tests indicate that the TEF deflection angle of the active rotor equipped with this actuator can reach ±4.3°. Subsequently, based on the controlled autoregressive moving average (CARMA) model, an adaptive controller is developed to reduce vibrations in the active rotor by using a minimum variance direct self-tuning regulator (MVSTDR). Finally, an unmanned helicopter is retrofitted with the active rotor, and vibration control experiments are performed under tethered hover conditions with vertical cabin vibration as the control target. Experimental results demonstrate the effectiveness of the designed actuator and the MVSTDR for vibration reduction on the helicopter equipped with an active rotor, which also validates the feasibility of active rotors for practical engineering applications in helicopter vibration control.

Keywords: helicopter; active rotor; trailing-edge flaps (TEFs); vibration suppression; piezoelectric actuator; adaptive vibration controller

1. Introduction

Helicopters are challenged by excessive vibrations, which adversely affect the fatigue life of structural components and the comfort of the crew and passengers. An active rotor with TEFs is an effective and proven vibration control technique for helicopters [1,2]. This method is implemented by actuating the TEFs installed on the rotor blade at higher harmonic frequencies to manipulate the aerodynamic load distribution and aeroelastic response of the rotor, thereby reducing helicopter vibrations [3,4]. The output of the actuator directly determines the TEF deflection angle and consequently influences the vibration control performance of the active rotor. Therefore, the actuator and its corresponding motion control law for driving the TEFs are the two core components of the active rotor.

Due to the advantages of fast dynamic response, high output force density and wide-band operating bandwidth, piezoelectric actuators have been widely used in active rotors for vibration control. Based on the inverse piezoelectric effect, piezoelectric actuators

Check for updates

Received: 6 February 2026
Revised: 18 March 2026
Accepted: 30 March 2026
Published: 1 April 2026

Copyright: © 2026 by the authors. Licensee MDPI, Basel, Switzerland. This article is an open access article distributed under the terms and conditions of the Creative Commons Attribution (CC BY) license.

realize electromechanical energy conversion and mechanical actuation. The direct actuation displacement of the piezoelectric materials is typically extremely small, so a suitable mechanical amplification mechanism is required to amplify their output displacement for driving the piezoelectric actuators used in the active rotors. Chopra et al. [5–8]. designed a piezoelectric bimorph actuator for TEF actuation that achieved a $\pm 5.5^\circ$ deflection angle under non-rotating conditions, and subsequent wind tunnel tests validated its favorable vibration control authority for the active rotor. The energy density of the piezoelectric bimorph actuator is inherently limited, as it employs the d_{31} coefficient of piezoelectric materials, which is significantly lower than the d_{33} coefficient. Lee et al. [9] developed a piezoelectric double-lever (L-L) actuator, using a lever mechanism to amplify the output displacement of the piezoelectric stack. Petitniot et al. [10] conducted wind tunnel tests of the active rotor using the APA500 actuator. Double-lever and APA500 actuators require the application of a bias voltage, which causes the output end to move away from the initial position. Therefore, once the piezoelectric stacks malfunction, the TEF may reach its maximum deflection, compromising the balance of the helicopter rotor. Fulton et al. [11] proposed a piezoelectric conformal actuator, which achieved a TEF deflection of 3° at a rotor rotational speed of 900 RPM. However, during the experiments, it was observed that the actuator exhibits inadequate reliability under the maximum driving voltage. Clement et al. [12,13] designed a piezoelectric C-block actuator, which amplifies the output displacement of the piezoelectric material by virtue of its own inherent structural configuration. In benchtop tests, this actuator enabled the TEF to attain a deflection angle exceeding 8°. However, the special flexural structure renders this actuator difficult to fabricate and manufacture. Tzianetopoulou [14] developed a piezoelectric double-X-frame actuator, which realizes bidirectional output through the opposite actuation of its two X-frame units. Prechtl et al. [15,16] and Straub et al. [17,18] carried out vibration control tests on the Mach-scaled rotor model of the CH-47D helicopter and the SMART rotor equipped with this actuator, respectively. This design remains highly promising, despite the potential friction problems caused by the rolling contact of the two independent X-frame units. Based on the double-X-frame actuator, Zhou et al. [19] proposed a compact piezoelectric double-acting actuator for a 4 m diameter helicopter rotor and assessed its performance through benchtop tests. In general, although the aforementioned piezoelectric actuators have been experimentally validated, there remains certain scope for further optimization of actuators employed in active rotors.

Beyond the mechanical design of the actuator, the motion control for the actuation, which refers to that for the active rotor, also plays a critical role in reducing vibrations of the helicopter active rotor. The Continuous-Time Higher Harmonic Control (CTHHC) algorithm has served as the dominant approach for closed-loop vibration control in previous studies of active rotors [2,20–23]. In addition, Spencer et al. [24] validated the effectiveness of the neural network algorithm in reducing rotor vibrations through wind tunnel tests on the active rotor under the hover condition. Yang et al. [25] performed simulations of the Mixed-Sensitivity H_∞ controller on an EC-145 helicopter equipped with TEFs, and the results indicated that a 70% vibration reduction was achieved. The CTHHC algorithm exhibits excellent vibration reduction performance for active rotors. However, this method is susceptible to instability induced by phase hysteresis, and may even amplify rotor vibrations due to control gain mismatch [26]. Neural network and Mixed-Sensitivity H_∞ algorithms are limited to wind tests in hover and numerical simulations, respectively.

The self-tuning regulator, an adaptive control method, is a promising candidate for vibration control in active rotors and has been successfully applied to other engineering fields. This control technique is commonly implemented for position tracking and velocity tracking [27–29]. In addition, the self-tuning regulator has also been applied to vibration

control. Zhang et al. [30] presented a minimum variance self-tuning regulator (MVSTR) for vibration control of a giant magnetostrictive actuator. Both numerical simulations and experimental tests showed that vibrations may be reduced up to more than 90%. Soni et al. [31] proposed a simple yet effective self-tuning controller to control vibrations of flexible rotors supported by active magnetic bearings, which was validated through a comparison between the optimal and self-tuning control. Li et al. [32] developed a self-tuning optimal controller for vibration suppression of magnetorheological (MR) semi-active suspension, and its effectiveness was validated through simulations and experiments based on a quarter-vehicle model incorporating the MR damper. These encouraging results have motivated us to investigate the implementation of the self-tuning regulator for active helicopter rotors.

In this study, an improved double-acting piezoelectric actuator is presented for full-scale active rotor blades to actuate the TEFs. A 6 m diameter helicopter rotor is designed and benchtop tests are conducted to assess the static deflection performance of the TEFs. Subsequently, the MVSTDR algorithm is introduced for the active rotor to reduce helicopter vibrations. Finally, vibration control experiments are performed on an unmanned helicopter retrofitted with an active rotor. Experimental results demonstrate the effectiveness of the established MVSTDR control algorithm for vibration reduction of the unmanned helicopter platform.

2. Active Rotor with TEFs

2.1. Improved Double-Acting Actuator

Based on the double-acting actuator proposed in Ref. [19], further design optimization was performed, and the improved double-acting piezoelectric actuator is presented in Figure 1. This actuator mainly consists of eight piezoelectric stack assemblies and two mechanical frames. Each assembly is composed of 5 commercially available piezoelectric stacks with dimensions of 8 mm × 8 mm × 18 mm. The piezoelectric stack information is shown in Table 1.

The piezoelectric stacks operate in the d_{33} mode, and thus, the axial strain equation of piezoelectric materials is given by

$$S_3 = S_{33}^E T_3 + d_{33} E_3 \tag{1}$$

where S_3 is the axial strain, T_3 is the axial stress, E_3 is the axial electric field, S_{33}^E is the elastic compliance constant, and d_{33} is the piezoelectric strain constant. For a stack with thickness t and cross-sectional area A, assuming small deformations, the following approximations and definitions are adopted:

$$\begin{cases} S_3 = \Delta t / t \\ T_3 = F / A \\ E_3 = V / t \end{cases}$$

where Δt, F, and V are the piezoelectric displacement, applied axial force, and voltage, respectively.

Substituting the above expressions into Equation (1), the displacement of the single piezoelectric stack is derived as

$$\Delta t = d_{33} V + \frac{S_{33}^E t}{A} F \tag{2}$$

Therefore, the output displacement ΔL of a piezoelectric stack assembly with n stacks is expressed as

$$\Delta L = nd_{33}V + \frac{nS_{33}^{E}t}{A}F \tag{3}$$

During installation of the TEF actuator, the axial force applied to the piezoelectric stack is the preload force, which is set to a very small value. Therefore, the piezoelectric deformation induced by the axial force can be neglected.

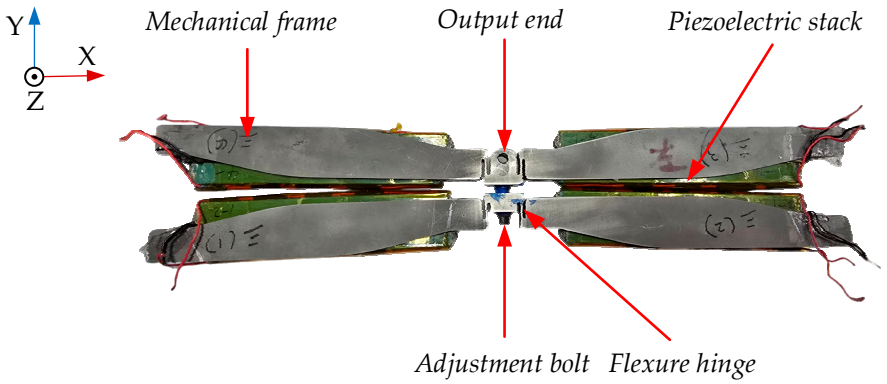


Figure 1. Improved double-acting piezoelectric actuator.

Table 1. Information of the piezoelectric stack.

Source	Piezomechanik GmbH company Munich, Germany
Type	Hard
Dimensions (mm)	$18 \times 8 \times 8$
Longitudinal piezoelectric coefficient d_{33} (pm/V)	635
Transverse piezoelectric coefficient d_{31} (pm/V)	-290
Mechanical quality factor	70
Elastic compliance constant S_{33}^{E} (m^2/N)	18×10^{-12}
Dielectric constant	5400

Since the displacement generated by the piezoelectric stack is extremely small, a mechanical mechanism must be designed to amplify its displacement. As shown in Figure 1, the flexure hinge is the key of the actuator, which is used to connect the mechanical frame with the output end. The compressive preloads exerted on the piezoelectric stacks can be adjusted by means of the adjustment bolt. The bore at the actuator's output end serves to connect the actuator to the TEF via a straight pin. Compared to the actuator developed in Ref. [19], this improved actuator removes the outer and several screws, which greatly simplifies its mechanical structure and further enhances its safety under rotational operation conditions. Moreover, its manufacturing and assembly processes are also simplified. These improvements are vital to promote the feasibility of the double-acting piezoelectric actuator in active rotor applications.

The schematic diagram of piezoelectric stack placement is shown in Figure 2. This piezoelectric actuator is constructed with four independent X modules, and each has two piezoelectric stacks. Mechanically, these two stacks are connected in series, whereas electrically they are connected in parallel.

The X module is presented in Figure 3. The piezoelectric stacks integrated into each X module elongate under voltage excitation, actuating the TEF to deflect precisely. With the slight elastic deformation neglected, the lengths of the frame BD, frame AC and flexible sheet CD are regarded as constant during actuator operation. Simultaneously, points A and C of the mechanical frame are fixed, and point B moves upward.

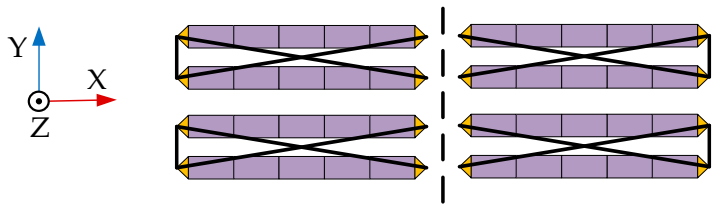


Figure 2. Schematic diagram of piezoelectric stack placement.

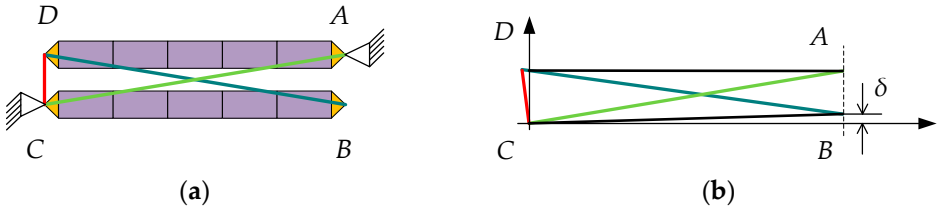


Figure 3. X module: (**a**) Schematic diagram of the X module; (**b**) Simplified model of the X module.

According the previous motion characteristics, the amplification ratio of the X module can be defined as

$$Amp_X = \frac{\delta}{\Delta L} = \frac{L}{H} \tag{4}$$

where δ is the displacement of point B, ΔL is the elongation of BC, and L and H are the lengths of BC and CD, respectively.

The four X modules are divided into upper and lower groups, as illustrated in Figure 4. On the basis of the same bias voltage, the amplitudes of the driving voltages applied to the two groups of X modules are identical, but their phases differ by 180°, enabling the TEF to achieve symmetric deflection. Therefore, the amplification ratio of the double-acting piezoelectric actuator is given by

$$Amp_{act} = \frac{2L}{H} \tag{5}$$

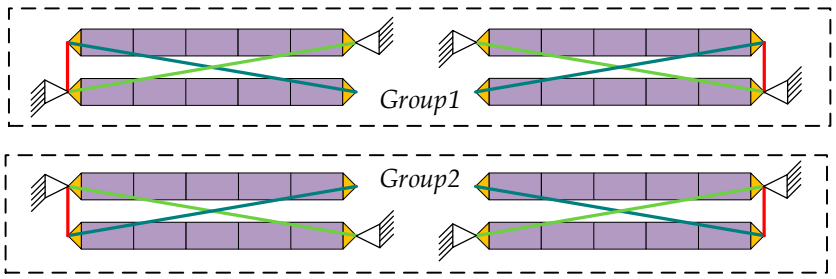


Figure 4. Piezoelectric stack grouping.

As the driving voltage applied to Group 1 increases, the driving voltage applied to Group 2 decreases, resulting in the active upward motion of the TEF; conversely, the TEF undergoes active downward deflection. When the driving voltages of Group 1 and Group 2 return to the bias value, the TEF resets to the neutral position. The coordinated control of the two groups of X modules enables push/pull motion of the TEF.

2.2. Rotor Blade

In order to evaluate the adaptive vibration reduction performance of the active rotor in the actual helicopter, a full-scale rotor blade was designed. The rotor parameters are listed in Table 2. It is a two-bladed rotor with two trailing-edge flaps on each blade, actuated by the designed double-acting piezoelectric actuator.

Table 2. Rotor parameters.

Parameters	Value
Rotor radius R/m	3.15
Number of blades N_b	2
Chord length c/m	0.18
Operating speed Ω/(r/min)	540
TEF_{inner} radial position	0.66R–0.77R
TEF_{inner} chord length (mm)	42
TEF_{outer} radial position	0.89R–0.97R
TEF_{outer} chord length (mm)	45

The active rotor blade is presented in Figure 5. The base blade is composed of a high-density foam core encased in a fiberglass composite skin. Fixing frames are pre-embedded to mount the TEFs and their actuation mechanisms. The TEF was designed with carbon fiber skin and an aluminum alloy frame. In the fabrication process of the TEFs, a high-precision CNC machine was employed to ensure dimensional accuracy, minimizing the gap between the TEF and the base blade and thereby guaranteeing the vibration control performance of the active rotor. Moreover, lead-edge counterweight was used to ensure that the section gravity center of the blade lies at the quarter chord.

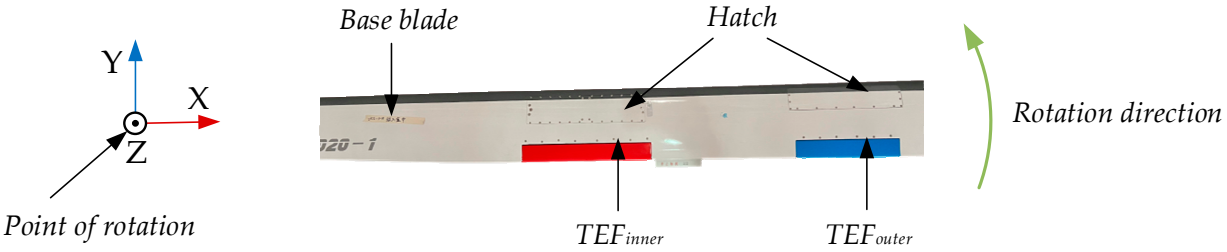


Figure 5. Active rotor blade.

As shown in Figure 6, benchtop tests of the active blade were conducted to assess the performance of TEFs and their actuation mechanisms. Control inputs generated by the signal generator were transmitted to the amplifier. And then the amplified voltage signals were sent to the actuation system to drive the TEFs. Meanwhile, the DC power was supplied to the Hall sensors mounted between the base blade and the TEF. The DAQ device was utilized to acquire the TEF deflection signals. As depicted in Figure 7, the static deflection angles of $\pm 4.3^\circ$ and $\pm 2.8^\circ$ were achieved for the inner TEF and outer TEF, respectively. Frequency sweep tests were carried out to estimate the transfer functions of the TEF system. Figure 8 indicates that there are no resonances in the frequency range of 1 Hz to 60 Hz. The fundamental frequency of this active rotor is 9 Hz (540 r/min) in hover experiments conducted on the unmanned helicopter. Accordingly, the TEF can operate at frequencies up to 6Ω (54 Hz).

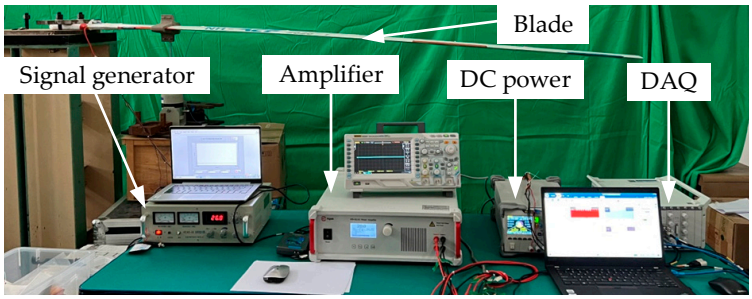


Figure 6. Benchtop tests of the TEF.

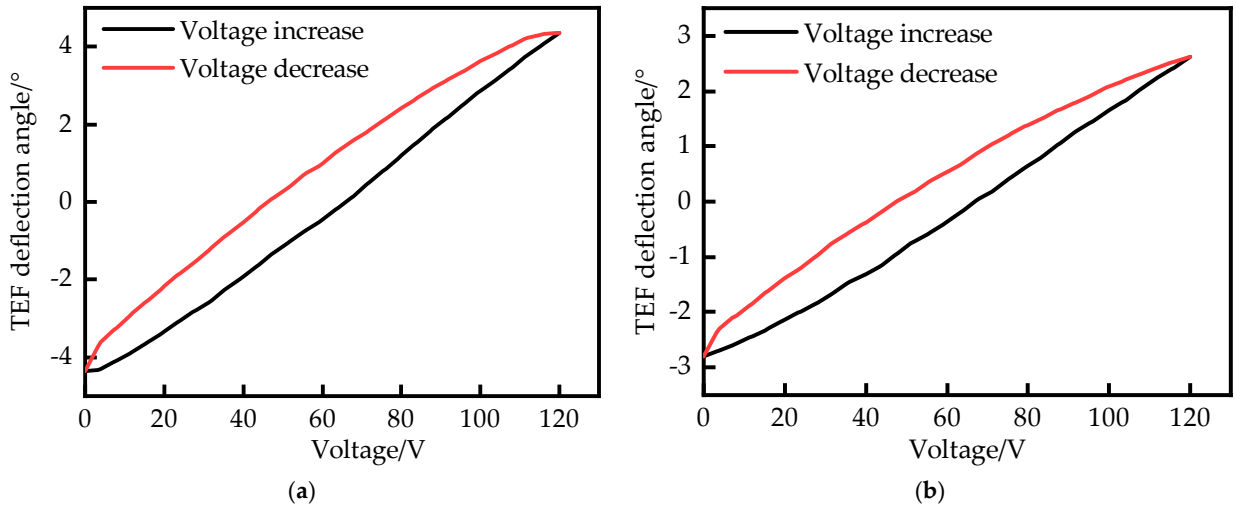


Figure 7. Static deflection angle of TEFs: (**a**) Inner TEF; (**b**) Outer TEF.

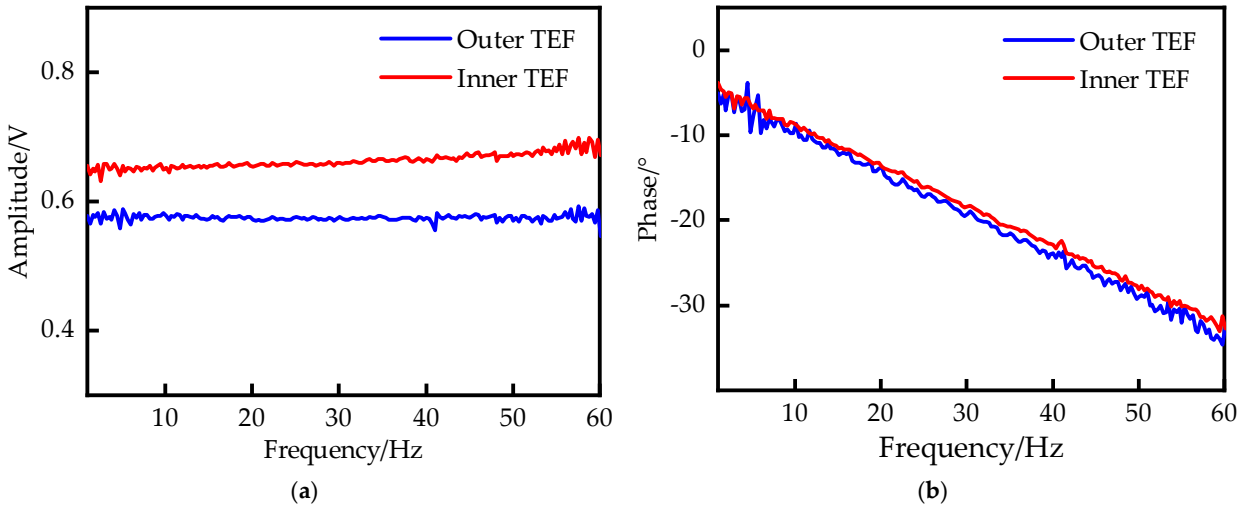


Figure 8. Frequency sweep tests: (**a**) Amplitude–frequency curves; (**b**) Phase–frequency curves.

Power consumption of the TEF deflection dictates the feasibility of applying the active rotor to the helicopter and achieve vibration reduction effects. According to the load transfer law of rotor hub, vibration loads exerted by the blade on the hub can be transmitted to the fuselage through the rotor hub at different harmonic frequencies. Therefore, the TEF control input voltage can be expressed as

$$U = Asin(2 \times \pi \times f + \varphi) + B \tag{6}$$

where U, A, B, f and φ are the control input voltage, the amplitude voltage, the bias voltage, the input phase and frequency, respectively. In this study, a two-bladed active rotor is employed. Consequently, the vibratory loads are dominated by the 2/rev harmonic component, with the control input frequency being 18 Hz. The power consumption of the outer TEF deflection at 18 Hz under the non-rotating condition for different input voltages is listed in Table 3.

Table 3. Power consumption of outer TEF under the non-rotating condition.

Amplitude/V	Bias/V	Power Consumption/w
10	10	11.9
20	20	25.5
30	30	42.5
40	40	58.5
50	50	74.9
60	60	93.9

3. Design of Adaptive Vibration Controller

3.1. Minimum Variance Self-Tuning Algorithm

In this study, the minimum variance self-tuning regulator (MVSTR) was adopted to suppress vibration of the active rotor for its algorithmic simplicity, ease of understanding and straightforward implementation. The architecture of the MVSTDR is shown in Figure 9. In this adaptive controller, a recursive extended least square (RELS) algorithm is employed to identify the parameters of the system model. And then the identified parameters and feedback output are transmitted to the control designer. Finally, as the designer runs, the control input is calculated by the minimum variance direct control law to reduce vibrations of the controlled plant.

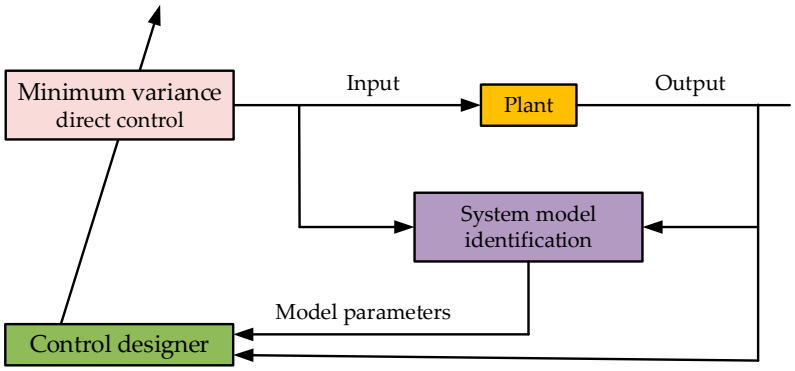


Figure 9. Block diagram of the minimum variance self-tuning regulator.

To ensure minimum variance of system output, the output must be first predicted, and the corresponding control law is subsequently acquired based on these predicted values. Thus, the CARMA model was adopted to characterize the active rotor system, which can be expressed as

$$A(z^{-1})y(k) = z^{-d}B(z^{-1})u(k) + C(z^{-1})\xi(k) \tag{7}$$

where $u(k)$, $y(k)$ and $\xi(k)$ are system input, system output and white noise, d is pure time delay, and $A(z^{-1})$, $B(z^{-1})$ and $C(z^{-1})$ are defined as

$$\begin{cases} A(z^{-1}) = 1 + a_1 z^{-1} + a_2 z^{-2} + \ldots + a_{n_a} z^{-n_a} \\ B(z^{-1}) = b_0 + b_1 z^{-1} + b_2 z^{-2} + \ldots + b_{n_b} z^{-n_b}, \ b_0 \neq 0 \\ C(z^{-1}) = 1 + c_1 z^{-1} + c_2 z^{-2} + \ldots + c_{n_c} z^{-n_c} \end{cases}$$

Both tracking accuracy and real-time computational efficiency of the control system are influenced by the CARMA model order n_a, n_b, n_c.

Predicted error of system output is written as

$$\widetilde{y}(k+d \mid k) = y(k+d) - \hat{y}(k+d \mid k) \tag{8}$$

where $y(k+d)$ and $\hat{y}(k+d \mid k)$ are actual output and predicted output at the time step $k+d$.

Taking the variance of the predicted error as the performance index, the minimum d-step optimal prediction output $y^*(k+d \mid k)$ should satisfy

$$C(z^{-1})y^*(k+d \mid k) = G(z^{-1})y(k) + F(z^{-1})u(k) \tag{9}$$

where

$$\begin{gathered} C(z^{-1}) = A(z^{-1})E(z^{-1}) + z^{-d}G(z^{-1}) \\ F(z^{-1}) = B(z^{-1})E(z^{-1}) \end{gathered} \tag{10}$$

and

$$\begin{cases} E(z^{-1}t) = 1 + e_1 z^{-1} \ldots + e_{n_e} z^{-n_e} \\ G(z^{-1}) = g_0 + g_1 z^{-1} \ldots + g_{n_g} z^{-n_g} \\ F(z^{-1}) = f_0 + f_1 z^{-1} + \ldots + f_{n_f} z^{-n_f} \end{cases}$$

With the control objective of tracking the desired output, the performance index function is given by

$$J = E\left\{ [y(k+d) - y_r(k+d)]^2 \right\} \tag{11}$$

where $y_r(k+d)$ is the desired output. Then, the control law of the minimum variance self-tuning regulator can be derived as

$$F(z^{-1})u(k) = C(z^{-1})y_r(k+d) - G(z^{-1})y(k) \tag{12}$$

Therefore, by combining Equations (4) and (12), the system structure of the MVSTR is illustrated in Figure 10.

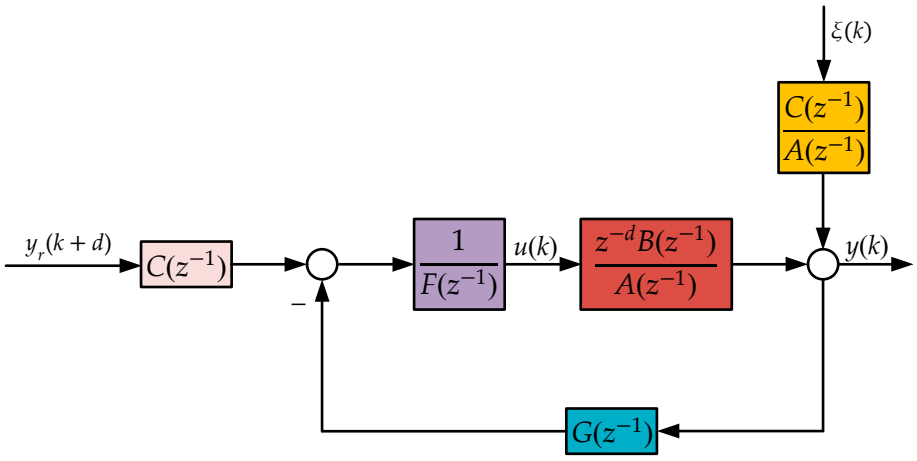


Figure 10. System structure of minimum variance control.

3.2. Control Law

In order to reduce the computational complexity of the MVSTR controller, a recursive algorithm is employed to directly estimate its parameters, and thus this control method is also referred to as the minimum variance self-tuning direct regulator (MVSTDR) controller. Equation (9) can be written in least square form:

$$\begin{aligned} y^*(k+d \mid k) &= Gy(k) + Fu(k) + (1-C)y^*(k+d \mid k) \\ &= \boldsymbol{\varphi}^T(k)\boldsymbol{\theta} \end{aligned} \tag{13}$$

where

$$\begin{aligned}\boldsymbol{\varphi}(k) = &\Big[y(k),\ldots,y\big(k-n_g\big),u(k),\ldots,u\Big(k-n_f\Big),\\ &-y^*(k+d-1\mid k-1),\ldots,-y^*(k+d-n_c\mid k-n_c)\Big]^T\\ \boldsymbol{\theta} = &[g_0,\ldots,g_{n_g},f_0,\ldots,f_{n_f},c_1,\ldots,c_{n_c}]^T\end{aligned}$$

According to Equations (7) and (10), it can be obtained that

$$y(k+d) = E\xi(k+d) + \frac{F}{C}u(k) + \frac{G}{C}y(k) \tag{14}$$

Combining Equations (9) and (10), the actual output $y(k+d)$ can be expressed as

$$y(k+d) = E\xi(k+d) + y^*(k+d\mid k) \tag{15}$$

Substituting Equation (9) into Equation (15), an estimation model for the MVSTDR controller is written as

$$y(k+d) = \boldsymbol{\varphi}^T(k)\boldsymbol{\theta} + E\xi(k+d) \tag{16}$$

By tracing back d steps of the actual output, Equation (16) can be rewritten as

$$y(k) = \boldsymbol{\varphi}^T(k-d)\boldsymbol{\theta} + \varepsilon(k) \tag{17}$$

where

$$\begin{aligned}\boldsymbol{\varphi}(k-d) = &\Big[y(k-d),\ldots,y\big(k-d-n_g\big),u(k-d),\ldots,u\Big(k-d-n_f\Big),\\ &-y^*(k-1\mid k-d-1),\ldots,-y^*(k-n_c\mid k-d-n_c)\Big]^T \epsilon R^{(n_g+n_f+2+n_c)\times 1}\\ \varepsilon(k) = E\xi(k) = &\xi(k) + e_1\xi(k-1) + \ldots + e_{d-1}\xi(k-1)\end{aligned}$$

Because the optimal predicted output in $\boldsymbol{\varphi}(k-d)$ is not observable, the estimated value $\hat{y}^*(k)$ replaces $y^*(k\mid k-d)$. Then, according to Equation (13), $\hat{y}^*(k)$ can be expressed as

$$\hat{y}^*(k) = \hat{\boldsymbol{\varphi}}^T(k-d)\hat{\boldsymbol{\theta}}(k-d) \tag{18}$$

where

$$\begin{aligned}\hat{\boldsymbol{\varphi}}(k-d) = &\Big[y(k-d),\ldots,y\big(k-d-n_g\big),u(k-d),\ldots,u\Big(k-d-n_f\Big),\\ &-\hat{y}^*(k-1),\ldots,-\hat{y}^*(k-n_c\,)\Big]^T\end{aligned}$$

At this point, the RELS algorithm is used to estimate $\boldsymbol{\theta}$ in Equation (17). The update rules are given by

$$\begin{cases}\hat{\boldsymbol{\theta}}(k) = \hat{\boldsymbol{\theta}}(k-1) + \boldsymbol{K}(k)\big[y(k) - \hat{\boldsymbol{\varphi}}^T(k-d)\hat{\boldsymbol{\theta}}(k-1)\big]\\ \boldsymbol{K}(k) = \frac{\boldsymbol{P}(k-1)\hat{\boldsymbol{\varphi}}(k-d)}{1+\hat{\boldsymbol{\varphi}}^T(k-d)\boldsymbol{P}(k-1)\hat{\boldsymbol{\varphi}}(k-d)}\\ \boldsymbol{P}(k) = \big[\boldsymbol{I} - \boldsymbol{K}\,(k)\hat{\boldsymbol{\varphi}}^T(k-d)\big]\boldsymbol{P}(k-1)\end{cases} \tag{19}$$

The choice of the initial covariance matrix $\boldsymbol{P}(0)$ is decisive for the convergence rate and stability of the controller parameters for identification. The value of $\boldsymbol{P}(0)$ is generally set as $\alpha\boldsymbol{I}$, where α ranges from 10^4 to 10^{10}.

Subsequently, based on the identified parameters (g, f, c), the control input u is calculated using Equation (12), which can be written as

$$u(k) = \frac{1}{\hat{f}_0}\left[-\sum_{i=1}^{n_f}\hat{f}_i u(k-i) + y_r(k+d) + \sum_{i=1}^{n_c}\hat{c}_i y_r(k+d-i) - \sum_{i=0}^{n_g}\hat{g}_i y(k-i)\right] \tag{20}$$

Moreover, in this study, the MVSTDR controller is designed for vibration suppression in the active rotor. Therefore, the desired output y_r is set to zero, so that Equation (20) can be simplified as

$$u(k) = \frac{1}{\hat{f}_0}[-\sum_{i=1}^{n_f} \hat{f}_i u(k-i) - \sum_{i=0}^{n_g} \hat{g}_i y(k-i)] \tag{21}$$

As can be seen from Equation (21), if $\hat{f}_0$ approaches zero, a divison-by-zero singularity arises, so a minimum value should be set for $\hat{f}_0$.

3.3. MVSTDR Stablility Analysis

To ensure the rigorous convergence of the MVSTDR, the following assumptions are imposed:

Assumption 1. *The plant is a minimum phase system, i.e., all zeros of* $B(z^{-1})$ *are inside the unit circle.* $C(z^{-1})$ *is strictly stable, with all zeros inside the unit circle.*

Assumption 2. $E[\xi(k)] = \mathbf{0}, E[\xi(k)^2] = \sigma^2 < \infty, \{\xi(k)\}$ *is a bounded, zero-mean white noise sequence.*

Assumption 3. *The regression vector* $\boldsymbol{\varphi}(k)$ *satisfies the persistent excitation.*

Assumption 4. *The parameter estimation* $\hat{\boldsymbol{\theta}}(k)$ *is uniformly bounded.*

According to Figure 10, the equation of the closed-loop system is derived as

$$y(k) = \frac{CBz^{-d}y_r(k+d) + CF\xi(k)}{AF + z^{-d}BG} \tag{22}$$

Combined with Equation (10), Equation (22) is transformed as

$$y(k) = \frac{CB[y_r(k) + E\xi(k)]}{CB} \tag{23}$$

Based on Assumption 1, Equation (23) is derived as

$$y(k) = y_r(k) + E\xi(k) \tag{24}$$

Due to the desired output y_r being set to zero in the MVSTDR, Equation (24) is written as

$$y(k) = E\xi(k) \tag{25}$$

Based on Assumption 2, $\xi(k)$ has finite variance. Thus, the output $\boldsymbol{y}(\boldsymbol{k})$ is uniformly bounded.

Considering that the desired output y_r is set to zero, Equation (12) is written as

$$F(z^{-1})u(k) = -G(z^{-1})y(k) \tag{26}$$

From Equations (10) and (26), the input $u(k)$ is rewritten as

$$u(k) = \frac{-G(z^{-1})\xi(k)}{B} \tag{27}$$

Since all zeros of $B(z^{-1})$ are inside the unit circle and $\xi(k)$ has finite variance, the input $u(k)$ is also bounded.

Substituting Equation (27) into Equation (13), $y^*(k+d|k) = \mathbf{0}$. Thus, $\varphi(k) = \hat{\varphi}^T(k)$. According to Ref. [33], the parameter estimation $\hat{\boldsymbol{\theta}}(\boldsymbol{k})$ of the RLS algorithm converges to the idea parameter vector $\boldsymbol{\theta}(k)$, hence

$$\boldsymbol{\theta}(k) - \hat{\boldsymbol{\theta}}(k) \xrightarrow{a.s.} 0 \tag{28}$$

Based on Equations (16) and (18), the prediction error of the MVSTDR can be expressed as

$$y(k+d) - \hat{y}^*(k+d) = \boldsymbol{\varphi}^T(k)\boldsymbol{\theta} - \boldsymbol{\varphi}^T(k)\hat{\boldsymbol{\theta}}(k) + E\xi(k+d) \tag{29}$$

From Equations (28) and (29), it follows that

$$y(k+d) - \hat{y}^*(k+d) \xrightarrow{a.s.} E\xi(k+d) \tag{30}$$

In general, under the assumptions of minimum phase, stable noise polynomial, persistent excitation, and bounded parameter estimation, the closed-loop system is globally asymptotically stable and achieves the optimal minimum variance performance, with inputs and outputs uniformly bounded.

4. Experimental Validation

4.1. Experimental Setup

The Z–5B/G unmanned helicopter (Nanjing Simulation Technology Research Institute, Nanjing, China) was utilized as the experimental platform, as shown in Figure 11. This helicopter features a conventional single main rotor and tail rotor configuration, equipped with a seesaw rotor hub. Both the rotor and fuselage are constructed from composite materials, and the helicopter is powered by a single piston engine, with a maximum takeoff weight of 500 kg and an extra power of 2000 W.

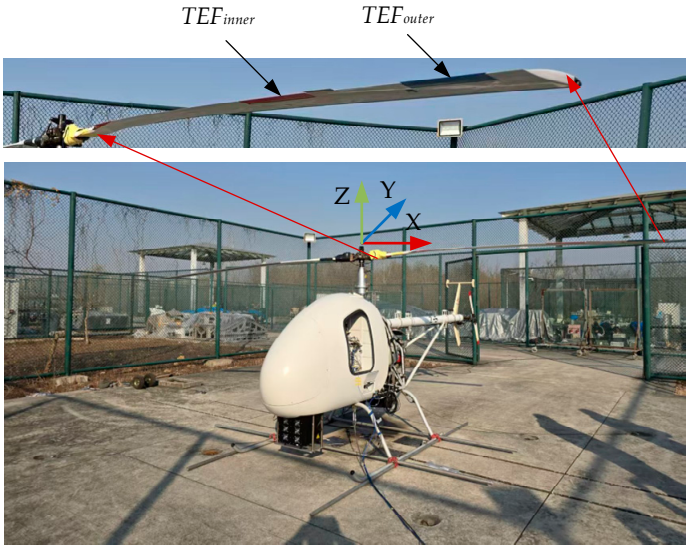


Figure 11. Unmanned helicopter experimental platform.

Based on this unmanned helicopter, the experimental platform was modified and upgraded, and a conventional rotor was replaced by the designed active rotor with TEFs (Figure 5). The TEFs are simultaneously actuated by the double-acting actuator, which can achieve push/pull motion. Additionally, the actuation system can ensure that the TEF reverts to the neutral position if the actuator malfunctions, which effectively avoids aerodynamic imbalance and guarantees the operating safety of the unmanned helicopter.

The schematic diagram of the active rotor for the vibration control experiment based on the unmanned helicopter is presented in Figure 12. According to the acceleration feedback signal, the real-time controller computes the corresponding TEF control signal using the MVSTDR algorithm. The control signal is amplified by a power amplifier and then transmitted to the actuator system, which actuates the TEF deflection. The data transfer of the acceleration sensing signal and actuation signal between the fixed and rotating frame is achieved through a slip ring mounted on the rotor shaft. Two accelerometers are installed at a key position of the helicopter's mission payload, as depicted in Figure 13a. One of them serves for vibration control feedback, while the other is dedicated to vibration monitoring to ensure the safety of the unmanned helicopter. The experimental setup photograph is shown in Figure 13b. During the implementation of vibration control for the unmanned helicopter, both the TEF control inputs and the acceleration outputs are logged by the NI compact RIO 9049 real-time controller (National Instruments, Austin, Texas, USA).

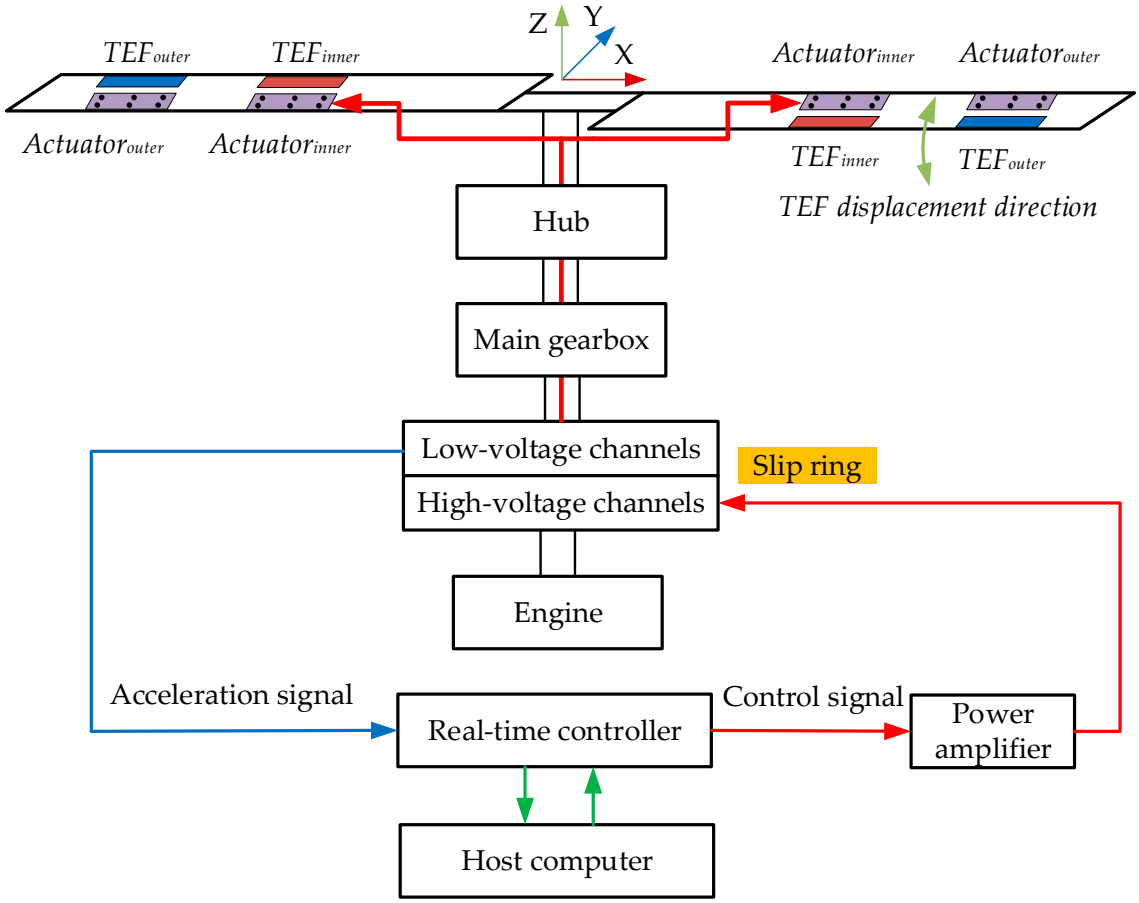
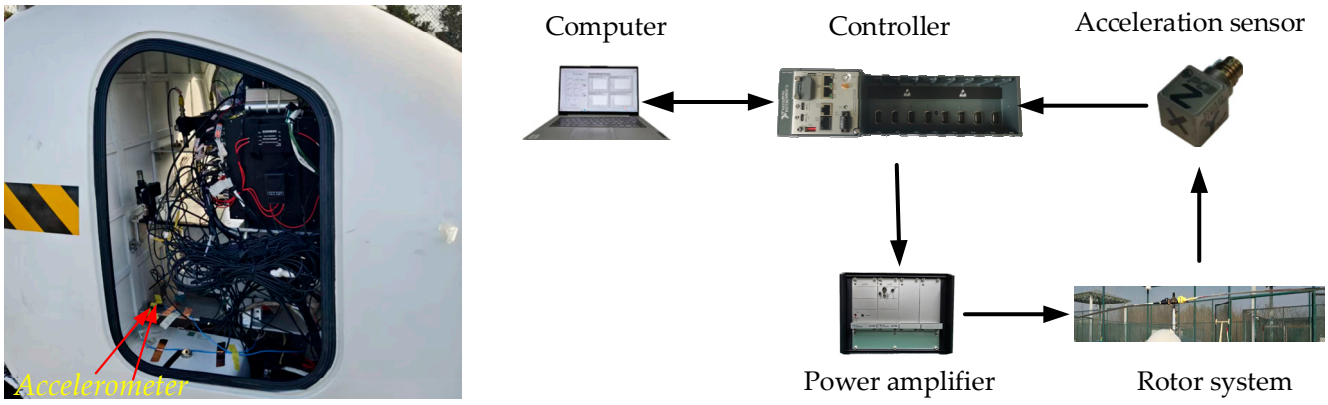


Figure 12. Schematic diagram of the active rotor with TEFs for vibration control.



(**a**) (**b**)

Figure 13. Vibration control system: (**a**) Accelerometer placement; (**b**) Experimental setup photograph.

4.2. Experimental Results

To further study the power consumption of TEF deflection under the rotating condition, the same input voltages as the non-rotating condition were used to deflect the outer TEF at 18 Hz. The power consumption results are presented in Table 4. As shown in Table 4, under rotating conditions, the power consumption is 81.7 W when the input voltage has an amplitude of 60 V, a bias of 60 V, and a frequency of 18 Hz (2/rev), which is slightly lower than that under non-rotating conditions. For the two-bladed active rotor, the power consumption is about 163.4 W. This unmanned helicopter platform can supply a maximum additional power of 2000 W to other equipment, which is much higher than the power consumption of the TEF actuation.

Table 4. Power consumption of single outer TEF under the operating condition.

Amplitude/V	Bias/V	Power Consumption/W
10	10	10.8
20	20	22.8
30	30	39.7
40	40	52.3
50	50	66.3
60	60	81.7

In this study, cabin vertical acceleration of the helicopter was designated as the vibration control target. Experiments on helicopter vibration control using the MVSTDR algorithm, implemented via LabVIEW, were conducted under the tethered hover condition. The block diagram of the MVSTDR algorithm for vibration reduction on the unmanned helicopter equipped with an active rotor is shown in Figure 14. Based on the TEF input signals and the measured acceleration signals, a CARMA model of the MVSTDR algorithm was identified. Simultaneously, the current TEF control input signals were obtained by combining identified model parameters, acceleration signals, and previous TEF input signals. For parameter identification of the CARMA model, band-limited white noise within the frequency of 1–40 Hz was generated by the real-time controller, covering harmonic components of the rotational frequency from 1/rev to 2/rev. Once the parameter identification of the helicopter system was completed, the MVSTDR controller was implemented on the unmanned helicopter with an active rotor.

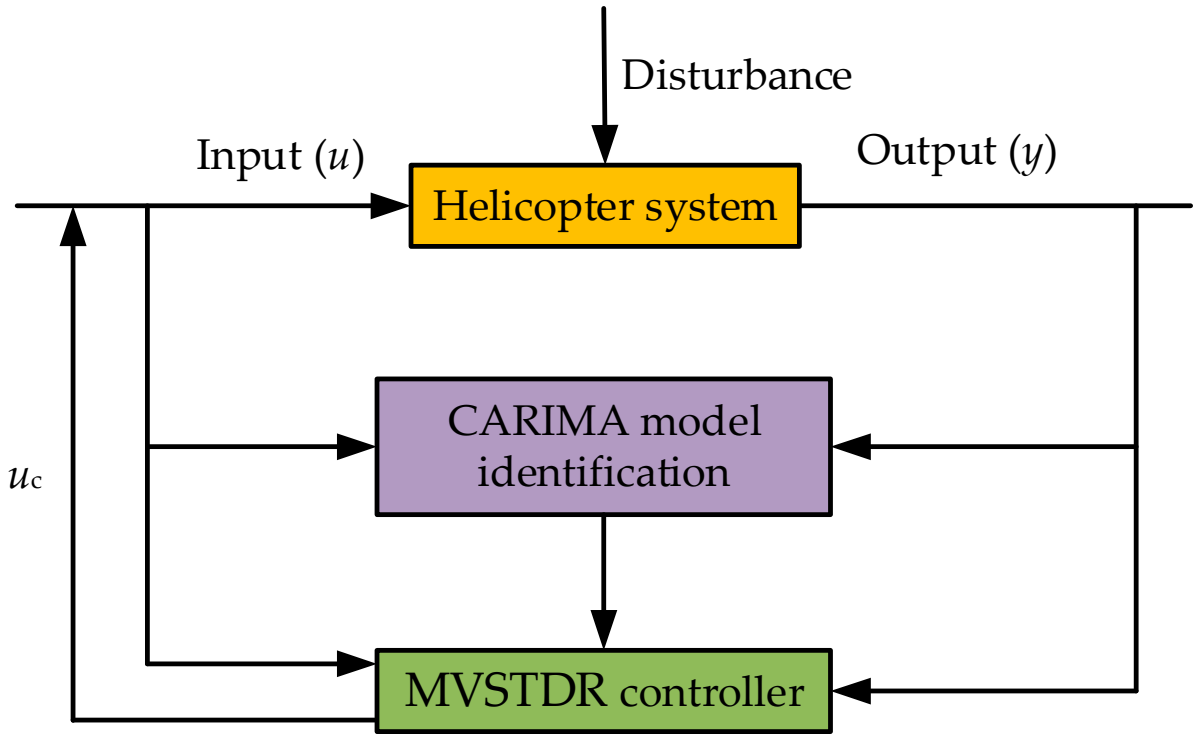


Figure 14. Block diagram of the MVSTDR for vibration reduction on the helicopter equipped with an active rotor.

In the MVSTDR implementation for vibration control, the model orders were set to $n_a = 4$, $n_b = 3$, $n_c = 1$. The initial covariance matrix $\boldsymbol{P}(0)$ was configured as $10^6\boldsymbol{I}$, and the minimum value of $\hat{f}_0$ was set to 10^{-3}. Figure 15 shows the process parameters (g, f, c) of the MVSTDR controller in vibration reductions. The parameters g_0, g_1, g_2, f_0, f_1, f_2 and c_1 in 2/rev vibration control of helicopter cabin converge to the values -0.1526, -0.0706, 0.0954, 0.0394, 0.1613, -0.0969 and 0.0613, respectively. The parameters g_0, g_1, g_2, f_0, f_1, f_2 and c_1 in 1/rev vibration control of helicopter cabin converge to the values -0.3028, 1.0089, -0.9914, 0.0291, -0.0304, 0.0982 and -0.4931, respectively. During the identification process of vibration control for the unmanned helicopter cabin, the control parameters exhibit a time-varying behavior instead of converging to a stable value from the outset. For 2/rev and 1/rev vibration control, the parameters converge to steady-state values after approximately 0.4 s and 0.2 s, respectively.

Given that the active rotor and the established vibration control strategy are novel techniques for the unmanned helicopter platform, all vibration control experiments were performed under tethered hover conditions to guarantee operational safety. The vibration reduction results of 2/rev and 1/rev vertical acceleration are shown in Figure 16. As can be seen from Figure 16a, when the MVSTDR controller is turned on, the 2/rev cabin vertical acceleration of the unmanned helicopter is suppressed significantly. Frequency-domain analysis was conducted to further confirm the vibration reduction effect and assess the side effect of the implementation of the MVSTDR controller. Figure 16b shows that a 66.9% (9.6 dB) vibration reduction is achieved for the 2/rev vertical acceleration response without any observed vibration amplification at other harmonic components.

Moreover, 1/rev vertical vibration control experiments were also carried out to expand the application of the active rotor with TEFs to address vibrations arising from rotor unbalance. As illustrated in Figure 16c,d, 1/rev harmonic vibrations of the unmanned helicopter cabin are markedly attenuated and the vibration reductions reach 75.5% (12.9 dB). Moreover, vibrations of other harmonic components are virtually unaltered. Noticeably, helicopter vibrations at 2/rev and 1/rev harmonic components are suppressed dramatically without any adjustments to the controller parameters or the system hardware. This represents a critical advantage of active rotors compared with traditional passive vibration control methods.

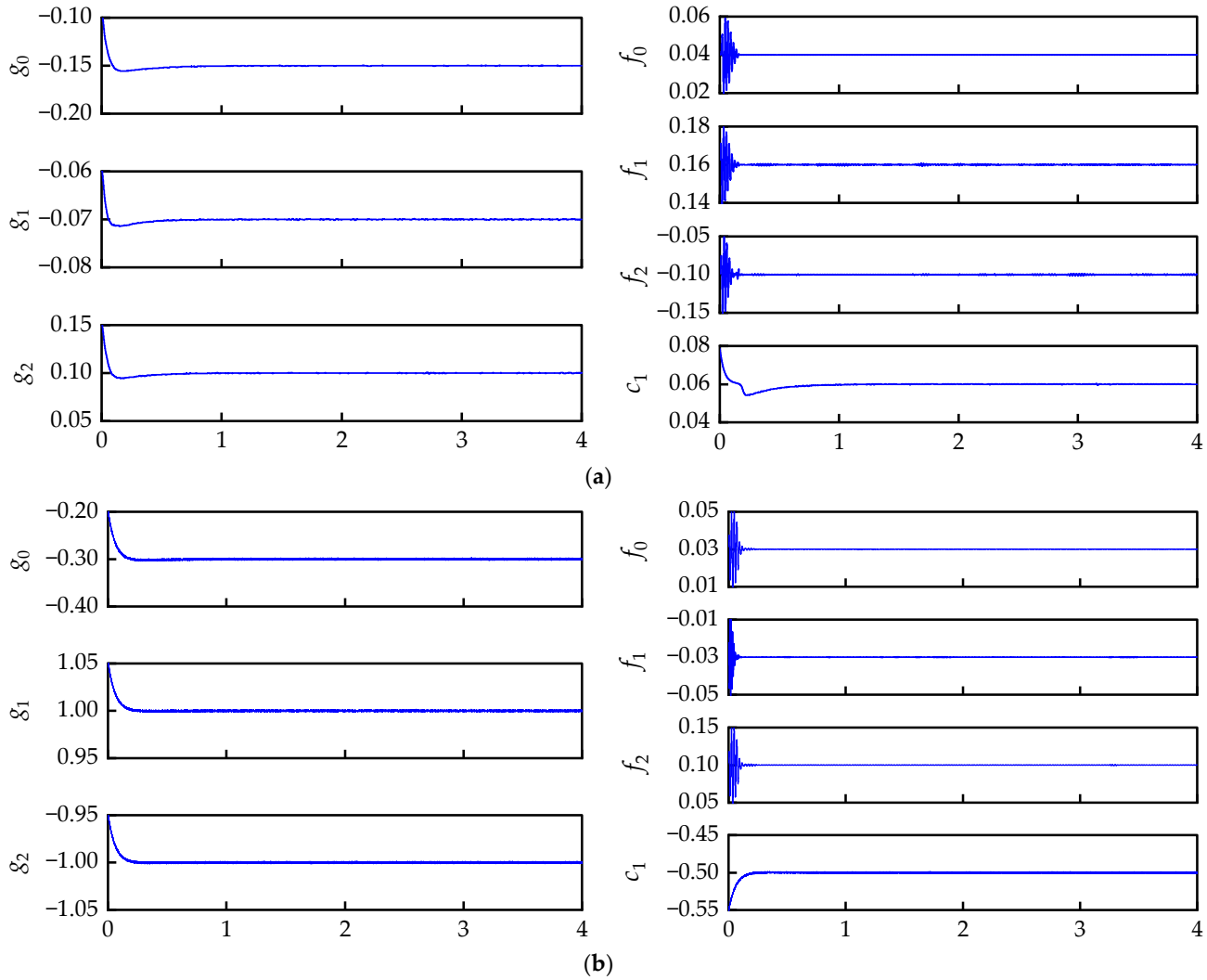


Figure 15. Process parameters in vibration reduction: (**a**) Parameters of 2/rev; (**b**) Parameters of 1/rev.

In addition, the successful implementation of the MVSTDR controller also implies that the designed improved double-acting piezoelectric actuator is effective for TEF actuation in the active rotor. Although the active rotor is equipped with two TEFs on each blade, significant vibration reductions was achieved solely with the outer TEF, demonstrating that the active rotor delivers sufficient vibration control authority. Therefore, combined with the developed control strategy, the software and hardware system of this active rotor can suppress vibrations of the unmanned helicopter platform, which further validates its feasibility in active control of helicopter vibrations.

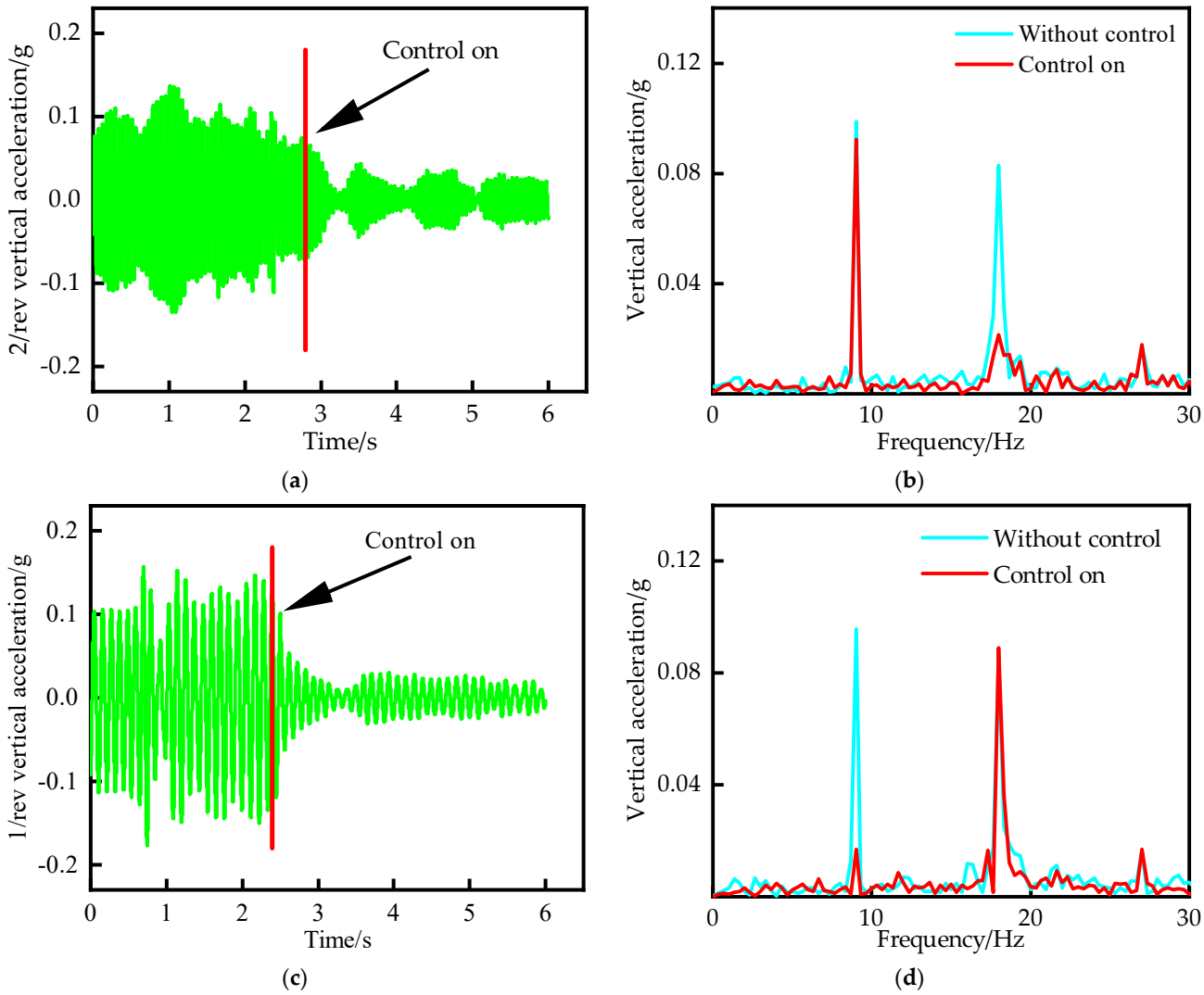


Figure 16. Vibration reductions of the helicopter in tethered hover: (**a**) 2/rev vertical acceleration in time domain; (**b**) 2/rev vertical acceleration in frequency domain; (**c**) 1/rev vertical acceleration in time domain; (**d**) 1/rev vertical acceleration in frequency domain.

5. Conclusions

An improved double-acting piezoelectric actuator for TEF actuation was designed, and the corresponding TEF deflection performance was evaluated through benchtop tests. Based on the CARMA model, an MVSTDR controller for the active rotor was established, and its vibration reduction performance was experimentally validated on an unmanned helicopter with an active rotor under tethered hover conditions. Several conclusions were obtained as follows:

1. The designed actuator was fabricated and subsequently integrated into the active rotor for TEF actuation, with static deflection angles of $\pm 4.3^\circ$ and $\pm 2.8^\circ$ for the inner and outer TEFs respectively, which lays a foundation for the subsequent vibration control experiments based on the active rotor.
2. The MVSTDR controller exhibits significant vibration reduction for 1/rev and 2/rev harmonic components in the cabin of the unmanned helicopter. The vertical vibrations at 2/rev and 1/rev were reduced by 66.9% (9.6 dB) and 77.5% (12.9 dB) respectively, demonstrating the superior vibration control performance of the developed control strategy.

3. The vibration control experiments conducted on the unmanned helicopter validate the feasibility and effectiveness of the designed double-acting piezoelectric actuator for the active rotor. Furthermore, the active rotor was successfully implemented on the unmanned helicopter platform, revealing its promising potential for practical engineering applications.

Author Contributions: Conceptualization, X.G.; methodology, X.G.; software, X.G.; data processing, X.G.; validation, L.D.; writing—original draft preparation, X.G.; writing—review and editing, J.Z.; supervision, W.Y.; project administration, L.D.; funding acquisition, J.Z. All authors have read and agreed to the published version of the manuscript.

Funding: This research was funded by the National Key Laboratory of Helicopter Aeromechanics Foundation of China (2023-HA-LB-067-03), the Key Laboratory of Rotor Aerodynamics Foundation (RAL202302-6) and the Natural Science Foundation of Jiangsu Province (BK20241420).

Data Availability Statement: Data are available from the corresponding authors.

Conflicts of Interest: The authors declare no conflicts of interest.

Nomenclatures and Abbreviations

Nomenclatures	
d_{31}	Transverse piezoelectric coefficient (pm/V)
d_{33}	Longitudinal piezoelectric coefficient (pm/V)
S_{33}^{E}	Elastic compliance constant (m^2/N)
R	Rotor radius (m)
N_b	Number of blades
c	Chord length (m)
Ω	Operating speed (r/min)
rev	Revolution
Abbreviations	
TEF	Trailing-edge flap
CARMA	Controlled autoregressive moving average
MVSTDR	Minimum variance direct self-tuning regulator
APA	Amplified piezoelectric actuator
RPM	Revolutions per minute
MVSTR	Minimum variance self-tuning regulator
MR	Magnetorheological
RELS	Recursive extended least square

References

1. Friedmann, P.P. On-blade control of rotor vibration, noise, and performance: Just around the corner? *J. Am. Helicopter Soc.* **2014**, *59*, 1–37. [CrossRef]
2. Zhou, J.L.; Dong, L.H.; Yang, W.D. Experimental study on transfer functions of an active rotor under different flight conditions. *Chin. J. Aeronaut.* **2022**, *35*, 107–120. [CrossRef]
3. Wilbur, M.L.; Mirick, P.H.; Yeager, W.T.; Langston, C.W.; Cesnik, C.E.S.; Shin, S. Vibratory loads reduction testing of the NASA/ARMY/MIT active twist rotor. *J. Am. Helicopter Soc.* **2002**, *47*, 123–133. [CrossRef]
4. Padthe, A.K.; Friedmann, P.P. Simultaneous blade–vortex interaction noise and vibration reduction in rotorcraft using microflaps, including the effect of actuator saturation. *J. Am. Helicopter Soc.* **2015**, *60*, 1–16. [CrossRef]
5. Walz, C.; Chopra, I. Design and testing of a helicopter rotor model with smart trailing edge flaps. In Proceedings of the 35th Structures, Structural Dynamics and Materials Conference, Adaptive Structures Forum, Hilton Head, SC, USA, 21–22 April 1994; pp. 309–319. [CrossRef]
6. Koratkar, N.A.; Chopra, I. Analysis and testing of a Froude scaled helicopter rotor with piezoelectric bender actuated trailing edge flaps. *J. Intell. Mater. Syst. Struct.* **1997**, *8*, 555–570. [CrossRef]
7. Koratkar, N.A.; Chopra, I. Wind tunnel testing of a Mach-scaled rotor model with trailing-edge flaps. *Smart Mater. Struct.* **2001**, *10*, 1–14. [CrossRef]

8. Koratkar, N.A.; Chopra, I. Open-loop hover testing of a smart rotor model. *AIAA J.* **2002**, *40*, 1495–1502. [CrossRef]
9. Taeoh, L.; Chopra, I. Design of piezostack-driven trailing-edge flap actuator for helicopter rotors. *Smart Mater. Struct.* **2001**, *10*, 15–24. [CrossRef]
10. Petitniot, J.L.; Rochettes, H.M.; Leconte, P. Experimental assessment and further development of amplified piezo actuators for active flap devices. In Proceedings of the 8th International Conference on New Actuators, Bremen, Germany, 10–12 June 2002; pp. 296–299.
11. Fulton, M.V.; Gold, N.P.; Nielsen, G.E.; Mansur, M.H.; Tischler, M.H.; Domzalski, D.B. Development and hover testing of the active elevon rotor. In Proceedings of the 68th Annual Forum of the American Helicopter Society, Fort Worth, TX, USA, 1–3 May 2012; pp. 1074–1101.
12. Clement, J.W.; Brei, D.; Moskalik, A.J. Bench-top characterization of an active rotor blade flap system incorporating c-block actuators. In Proceedings of the 39th AIAA/ASME/ASCE/AHS/ASC Structures, Structural Dynamics, and Materials Conference and Exhibit, Long Beach, CA, USA, 20–23 April 1998; pp. 2857–2869. [CrossRef]
13. Clement, J.W.; Brei, D.; Barrett, R. Wind tunnel testing of a high authority airspeed insensitive rotor blade flap. In Proceedings of the 40th Structures, Structural Dynamics, and Materials Conference and Exhibit, St. Louis, MO, USA, 12–15 April 1999; pp. 2414–2424. [CrossRef]
14. Tzianetopoulou, T. Design of an Improved Piezoelectric Actuator for Helicopter Rotor Control. Ph.D. Thesis, Massachusetts Institute of Technology, Cambridge, MA, USA, 2001.
15. Prechtl, E.F.; Hall, S.R. Closed-loop vibration control experiments on a rotor with blade mounted actuation. In Proceedings of the 41st Structures, Structural Dynamics, and Materials Conference and Exhibit, Atlanta, GA, USA, 3–6 April 2000; pp. 1–15. [CrossRef]
16. Prechtl, E.F. Design and Implementation of a Piezoelectric Servo-Flap Actuation System for Helicopter Rotor Individual Blade Control. Ph.D. Thesis, Massachusetts Institute of Technology, Cambridge, MA, USA, 2000.
17. Straub, F.K.; Anand, V.R.; Bircgette, T.S.; Benton, H.L. SMART rotor development and wind tunnel test. In Proceedings of the 35th European Rotorcraft Forum, Hamburg, Germany, 22–25 September 2009.
18. Straub, F.K.; Kennedy, D.K.; Stemple, A.D.; Anand, V.R.; Bircgette, T.S. Development and whirl tower test of the SMART active flap rotor. In Proceedings of the SPIE's Intl Symposium on Smart Structures and Materials, San Diego, CA, USA, 29 July 2004; pp. 14–18. [CrossRef]
19. Zhou, J.L.; Dong, L.H.; Yang, W.D. A double-acting piezoelectric actuator for helicopter active rotor. *Actuators* **2021**, *10*, 247. [CrossRef]
20. Straub, F.K.; Anand, V.R.; Lau, B.H. Wind tunnel test of the SMART active flap rotor. *J. Am. Helicopter Soc.* **2018**, *63*, 1–16. [CrossRef]
21. Roth, D.; Enenkl, B.; Dieterich, O. Active rotor control by flaps for vibration reduction—Full scale demonstrator and first flight test results. In Proceedings of the 32nd European Rotorcraft Forum, Maastricht, The Netherlands, 12–14 September 2006.
22. Rabourdin, A.; Maurice, J.B.; Dieterich, O.; Konstanzer, P. Blue Pulse active rotor control at Airbus Helicopters—New EC145 demonstrator and flight test results. In Proceedings of the 70th Annual Forum of the American Helicopter Society, Montreal, QC, Canada, 20–22 May 2014.
23. Dieterich, O.; Rabourdin, A.; Maurice, J.B.; Konstanzer, P. Blue pulse: Active rotor control by trailing edge flaps at Airbus heli-copters. In Proceedings of the 41st European Rotorcraft Forum, Munich, Germany, 1–4 September 2015.
24. Spencer, M.G.; Sanner, R.M.; Chopra, I. Close-loop neurocontroller tests on piezoactuated smart rotor blades in hover. *AIAA J.* **2002**, *40*, 1596–1602. [CrossRef]
25. Yang, H.; Alotaibi, J.; Viviescas, R.M. Advanced on-bladed control for vibration reduction of the EC-145 helicopter: Robust principal components vs H-infinity. In Proceedings of the AIAA Scitech 2020 Forum, Orlando, FL, USA, 6–10 January 2020; pp. 6–10. [CrossRef]
26. Patt, D.; Liu, L.; Chandrasekar, J.; Bernstein, D.S.; Friedmann, P.P. Higher-harmonic-control algorithm for helicopter vibration reduction revisited. *J. Gui. Control Dyn.* **2005**, *28*, 918–930. [CrossRef]
27. Xi, X.C.; Ye, L.; Yu, J.H.; Zhao, W.S. Minimum-variance self-tuning regulator in EDM drilling processes for ultra-high-aspect-ratio small holes. *Int. J. Adv. Manuf. Technol.* **2020**, *111*, 3293–3303. [CrossRef]
28. Pradhan, S.K.; Subudhi, B. Position control of a flexible manipulator using a new nonlinear self-tuning PID controller. *IEEE/CAA J. Autom. Sinica.* **2018**, *7*, 136–149. [CrossRef]
29. Yuan, H.; Huang, D.Q.; Li, X.F. Adaptive speed tracking control for high speed trains under stochastic operation environments. *Automatica* **2023**, *147*, 110674. [CrossRef]
30. Zhang, T.; Yang, B.T.; Li, H.G.; Meng, G. Dynamic modeling and adaptive vibration control study for giant magnetostrictive actuators. *Sens. Actuators A Phys.* **2013**, *190*, 96–105. [CrossRef]
31. Soni, T.; Dutt, J.K.; Das, A. Self-tuning control of parametrically excited active magnetic bearing system due to harmonic base motion using fuzzy logic. *J. Vib. Control* **2022**, *29*, 1191–1204. [CrossRef]

32. Li, G.; Gan, Y.; Liu, Q.; Xie, M.J.; Huang, Q.S.; Zeng, L.P. Design and evaluation of self-tuning optimal control for vibration suppression of magnetorheological semi-active suspension. *J. Low Freq. Noise Vib. Act. Control* **2025**, *44*, 547–564. [CrossRef]
33. Ljung, L. Consistency of the least-squares identification method. *IEEE Trans. Autom. Control* **1976**, *21*, 779–781. [CrossRef]

Disclaimer/Publisher's Note: The statements, opinions and data contained in all publications are solely those of the individual author(s) and contributor(s) and not of MDPI and/or the editor(s). MDPI and/or the editor(s) disclaim responsibility for any injury to people or property resulting from any ideas, methods, instructions or products referred to in the content.